Shift-current bulk photovoltaic effect influenced by quasiparticle and exciton

Ruixiang Fei, Liang Z. Tan, and Andrew M. Rappe

Phys. Rev. B **101**, 045104 — Published 8 January 2020

DOI: 10.1103/PhysRevB.101.045104

Shift current bulk photovaltaic effect influenced by quasiparticle and exciton

Ruixiang Fei,[1] Liang Z. Tan,[2] and Andrew M. Rappe[1,*]

[1] *Department of Chemistry, University of Pennsylvania, Philadelphia, Pennsylvania 19104-6323, USA*
[2] *Molecular Foundry, Lawrence Berkeley National Laboratory, Berkeley, California 94720, United States*

We compute the shift current bulk photovoltaic effect (BPVE) in bulk $BaTiO_3$ and two dimensional monochalcogenide SnSe considering quasi-particle corrections and exciton effects. We explore changes in shift current peak position and magnitude reduction due to band renormalization. For BaTiO3, we demonstrate that shift current reduces near the band edge due to exciton effects. We find the calculated magnitude of shift current in $BaTiO_3$ is only half of that obtained in experiments, indicating that mechanisms other than shift current can contribute to BPVE. Additionally, we reveal that the shift current near band gap have very small change by exciton in two dimensional SnSe, suggesting that thin film is a feasible way to reduce the exciton effect on the shift current. These results suggest that many-body corrections are important for accurate assessments of bulk photovoltaic materials and to understand the mechanisms behind the BPVE.

I. INTRODUCTION

The bulk photovoltaic effect (BPVE), which has also been referred to as the "photogalvanic effect", is a resonant nonlinear process where photocurrent is generated in materials without space-inversion symmetry[1–5]. It motivates great interest in solar energy conversion in ferroelectric perovskites including $BaTiO_3$[6–8], $LiNbO_3$[9,10] and $BiFeO_3$[11–14], because the induced open-circuit voltage can be much larger than the band-gap energy[15–17]. The DC photocurrent can be contributed by several mechanisms, including the shift current[5,18–20], injection current[5,20], and the ballistic current[21–23]. However, up to date, the relative magnitudes of currents generated by those mechanisms are still under debate; the many-body effect, for instance, has been already recognized as an important part in the magnitudes of these exotic nonlinear photocurrents[5] but always neglected in computation, resulting in possible misunderstandings in these magnitudes. Therefore, deeper understanding of photovoltaic effects is crucial for the discovery and the design of new types of noncentrosymmetric semiconductors for BPVE application[18,24,25].

The shift current is the result of the real-space shift of the photo-excited conduction and valence Bloch electrons by a topological quantity, the Berry phase[5,26,27]. It is not sensitive to the carrier lifetime in compare with the injection current. Comparisons of the experimentally measured BPVE in ferroelectric $BaTiO_3$[7,8] and $BiFeO_3$[28] with first-principles DFT calculations[14,29] suggest that shift current is responsible for a dominant portion of the BPVE in ferroelectrics. However, as stated above, these conclusions, which rule out other mechanisms and the corresponding photocurrents, were drawn from calculations neglecting quasiparticle corrections and excitonic effects, and thus should be revised with these many-body effects taken into account. In this paper, we focus on the shift current BPVE and show the many-body effects can give rise to sizable corrections, which is crucial to understanding the dominant mechanism of BPVE and material design for BPVE application.

To demonstrate the influence of many-body effect in BPVE, we study the shift current with quasiparticle GW corrections and excitonic effects in the typical perovskite oxide $BaTiO_3$ and large BPVE two-dimensional monochalcogenide SnSe[30–32]. These many-body effects work to redistribute the spectral weight of the shift current response. In general, there is a tendency for the shift-current response to be reduced by the exciton effects, although the behaviors are different for bulk material and two-dimensional materials, as we show below.

The remainder of this paper is organized as follows: Section II demonstrates the shift current tensor with quasi-particle effect; Section III presents the glass coefficient with exciton effect for three-dimensional material. Section IV discuss the total shift current with exciton effect for two-dimensional material. Section V summarizes our studies and conclusions.

II. SHIFT CURRENT TENSOR WITH QUASI-PARTICLE EFFECT

The shift current is calculated within perturbation theory[5,29,33] with the monochromatic electric field treated classically, taking the form $E_s(t) = E_s(\omega)e^{i\omega t} + E_s(-\omega)e^{-i\omega t}$. The second order response function for the shift current includes transitions of electrons to all unoccupied bands,

$$\begin{aligned} j_Q(\omega) =& \sum_s \sigma_{ssQ}(0,\omega,-\omega)E_s(\omega)E_s(-\omega) \\ \sigma_{ssQ}(0,\omega,-\omega) =& \pi\frac{e^3}{\hbar^2}\int\frac{d\mathbf{k}}{4\pi^3}\sum_{nm} f_{mn}r_s(m,n,\mathbf{k}) \\ & \times r_s(n,m,\mathbf{k})R_Q(m,n,\mathbf{k})\delta(\omega_{mn}\pm\omega) \end{aligned} \tag{1}$$

where n and m are the band indices, $\mathbf{k}$ is the wave vector, $f_{mn} = f_m - f_n$ is the Fermi-Dirac occupation number, $\omega_{mn} = \omega_m - \omega_n$ is the band energy difference and σ_{ssQ} is a third-rank tensor giving current density J as a response to monochromatic electromagnetic field E.

The expression is composed of the effective position matrix elements $r_s(m,n,\mathbf{k})$ and the so-called "shift vector" $R_Q(m,n,\mathbf{k})$:

$$r_s(m,n,\mathbf{k}) \equiv \frac{v_s(m,n,\mathbf{k})}{i\omega_{mn}} = \frac{\langle m\mathbf{k}|v_s|n\mathbf{k}\rangle}{i\omega_{mn}}$$
$$R_Q(m,n,\mathbf{k}) = -\frac{\partial\phi(m,n,\mathbf{k})}{\partial k_Q} - (A_Q(n,n,\mathbf{k}) - A_Q(m,m,\mathbf{k})) \tag{2}$$

Here, $v(m,n,\mathbf{k})$ are velocity matrix elements, $A(m,m,\mathbf{k})$ are Berry connections for band m, and $\phi(m,n,\mathbf{k})$ is the phase of the momentum matrix element between bands m and n.

The wave functions and eigenvalues were generated using the plane-wave density functional theory (DFT) package Quantum ESPRESSO with the generalized gradient approximation (GGA) exchange correlation functional. Norm-conserving, designed nonlocal pseudopotentials[34,35] were produced using the OPIUM package. Quasiparticle corrections to the nonlinear conductivity σ were made by using GW-renormalized matrix elements[36] and quasiparticle energies in Eq. 1 (See Eq. S6 for details). The current density induced by an external light source depends not only on the nonlinear conductivity, but also on the attenuation of the light field within the material. To account for this effect, we consider corrections to the dielectric function at the GW+Bethe Salpeter Equation (BSE) level. The BSE

$$(E_{c\mathbf{k}} - E_{v\mathbf{k}})A^S_{vc\mathbf{k}} + \sum_{v'c'\mathbf{k}'} K_{vc\mathbf{k},v'c'\mathbf{k}'}(\Omega^S)A^S_{v'c'\mathbf{k}'} = \Omega^S A^S_{vc\mathbf{k}} \tag{3}$$

gives correlated e-h excitations S of energy Ω^S, expanded in the basis of e-h pairs $|S\rangle = \sum A^S_{vc\mathbf{k}}|vc\mathbf{k}\rangle$. Here, v and c stand for the valence and conduction band indices, respectively. K is e-h interaction kernel. The quasiparticle and excitonic effects are incorporated into shift-current calculation by interfacing our in-house shift current code[14,29] with the BerkeleyGW package[37,38]. For additional calculation information, see Appendix A.

We first perform first-principles DFT calculations of the shift current for $BaTiO_3$ (BTO), which derives from the cubic perovskite structure and is in a tetragonal ferroelectric phase at room temperature. We use experimental room temperature geometries, i.e. the tetragonal phase[39] for this calculation. The quasiparticle energies are calculated with the G_0W_0 approximation. Because the quasiparticle wavefunction is equal to the DFT wavefunctions at the first order, we do not update the wavefunctions for shift current tensor calculation at the GW level. In Fig 1 (a-c), we show the shift current tensor elements in the direction of material polarization (Z), and the shift vector integrated over the Brillouin zone $\bar{R}$ given by

$$\bar{R}_Z(\omega) = \sum_{nm}\int d\mathbf{k} R_z(m,n,\mathbf{k})\delta(\omega_m - \omega_n \pm \omega) \tag{4}$$

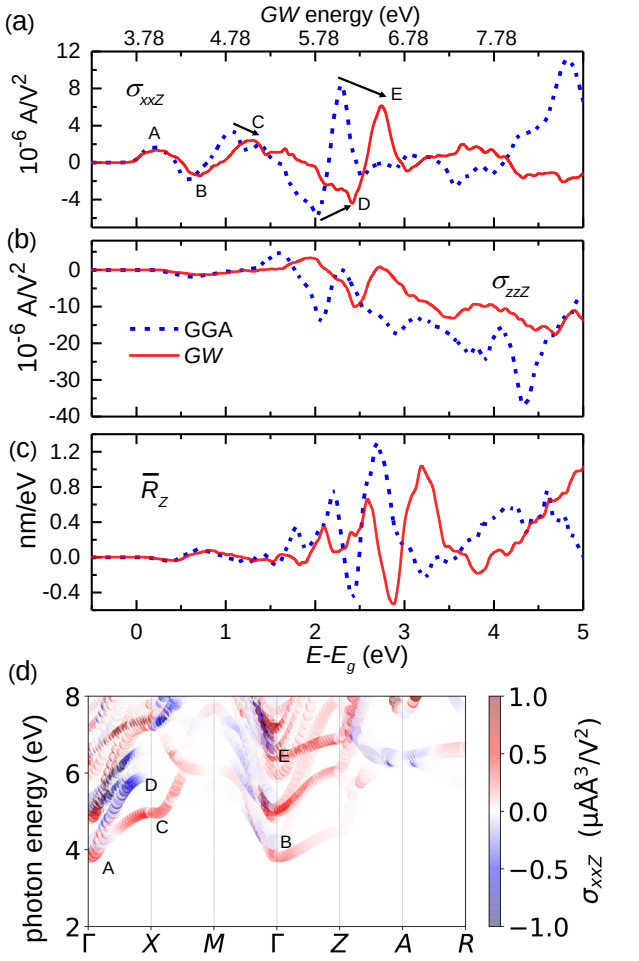

FIG. 1. The overall current susceptibility σ_{xxZ} (a), σ_{zzZ} (b) and aggregated shift vector $\bar{R}_Z$ (c) for $BaTiO_3$ as a function of energy above their respective band gaps. In each panel of (a-c), spectra are given at the GGA level (blue) and the GW level (red); the corresponding excitation energy of spectra at the GW level are given on the top. In (a), the arrows represent the corresponding peaks between GGA and GW levels. The k-resolved photocurrent σ_{xxZ} at the GW level (d), in which the color gives the value of the photocurrent response. The dominant contributions to the photocurrent peaks at the GW level are labeled in (d), corresponding to labeled peak in (a). The calculations adopt the experimental lattice constants at room temperature $a = b = 3.9998$ Å, and $c = 4.018$ Å.

The direct band gap at the GGA level is 2.10 eV, and the quasiparticle direct band gap is 3.78 eV, consistent with previous GW calculations[40]. To compare spectra at both GGA and GW levels, we plot the spectra as a function of energy above their respective band gaps. The peak of response is several eV above the band gap and well outside the visible spectrum, while the shift current at energies near the band gap is small.

GW corrections in general increase band gaps and bandwidths[41] in semiconductors. We therefore expect that the effect of GW corrections on a shift current spectrum is to shift and stretch the spectrum to higher fre-

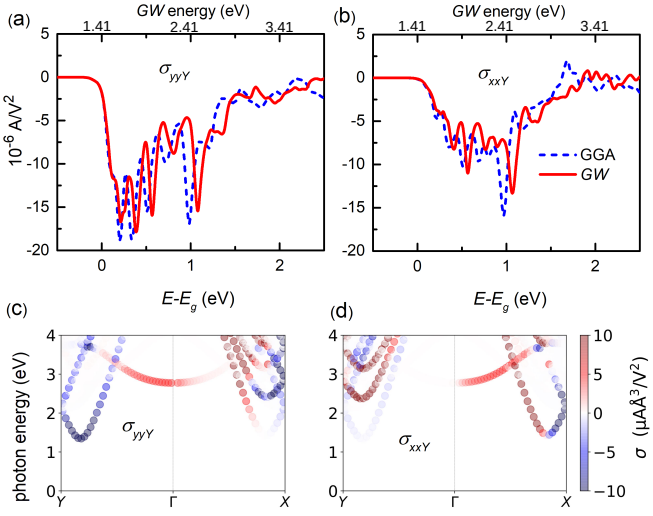

FIG. 2. The current susceptibility σ_{yyY} (a) and σ_{xxY} (b) for mono layer SnSe as a function of energy above their respective band gaps. In (a) and (b), spectra are given at the GGA level (blue) and GW level (red), and the correspond energy of spectra at the GW level are given on the top of each panel. The k-resolved photocurrent susceptibility σ_{yyY} (c) and σ_{xxY} (d) at the GW level. In (c) and (d), the color gives the value of the photocurrent response, and each direction valley in Brillouin zone can be optically pumped separately by excitation with linearly polarized light.

quencies. Peak position changes, indicated by arrows in Fig 1(a), are stronger at the high energy, but tiny at low energy (e.g. peak A). The corresponding k-space-resolved photocurrent tensor at the GW level is

$$\begin{aligned}\sigma_{ssQ}(k) =&\pi\frac{2e^3}{\hbar^2}\sum_{nm} f_{mn} r_s(m,n,\mathbf{k}) \\ &\times r_s(n,m,\mathbf{k}) R_Q(m,n,\mathbf{k})\delta(\omega_{mn}\pm\omega)\end{aligned} \tag{5}$$

We illustrated this k-space-resolved photocurrent in Fig 1(d) with colors representing the current direction. Besides the changes in the spectral peak position at the GW level, the magnitudes of the spectra after GW correction are smaller. Because of the bandwidth increase, the stretching of the spectrum distributes spectral weight over a greater spectral range, resulting in lower magnitudes of shift current. The GW increases the valence and conduction bandwidths by 22% and 20% for BTO, respectively, showing that the quasiparticle correction in BTO is important for accurate shift current spectra (see Appendix A).

Next, we apply this GW shift current analysis to the monolayer monochalcogenides, a class of room-temperature two-dimensional ferroelectrics[30,42]. We select SnSe as a prototype, which has large spontaneous polarization 0.3 C/m^2 in the Y direction[30,31] and large shift current susceptibility[31]. The GGA and GW band gaps of 0.92 eV and 1.41 eV are in the optimal range for solar cells[43,44]. There are large shift current responses under yy (Fig 2a) and xx (Fig 2b) polarized illumination within 1 eV above the band gap. Similar to BTO, We find that the GW shift current spectrum is shifted and stretched to higher frequencies, and the magnitudes after GW correction are smaller. However, the shift current response correction is weaker than that of bulk BTO. We attribute this to the smaller bandwidth correction for monolayer SnSe due to the stronger Coulomb screening, as the GW valence and conduction bandwidths increase by only 13% and 8%, respectively (see Appendix A). The shift current susceptibility σ_{xxY} near band gap is much smaller than σ_{yyY}, which can be understood from the k-resolved current susceptibility decribed by Eq. 5 (Fig 2c and 2d). The yy polarized light pumps more current for the y valley. Each valley in Brillouin zone can be separately pumped with linearly polarized light. Interestingly, different from the valley separated by circular-polarized light in MoS_2[45,46], here it is separated by linear-polarized light.

Generally, the bandwidth of most bulk semiconductors is underestimated by more than 10% at DFT level, while GW gives a more accurate bandwidth[41,47]. So the quasiparticle correction is suggested for shift current especially for the high-energy photon. On the other hand, the quasiparticle correction for shift-current of two-dimensional materials to be strong is not guaranteed, suggesting a case-by-case analysis of the quasipaticle correction on shift current.

III. GLASS COEFFICIENT WITH EXCITON EFFECT FOR THREE DIMENSIONAL FERROELECTRICS

Next, we analyze the impact of the excitons on absorption and reflectivity, and their effect on shift current. The total current in the direction normal to light incidence is

$$\begin{aligned}J_{ssQ} &= \frac{K_{ssQ}}{\alpha_{ss}(\omega)}(1-R_{ss})(1-e^{-\alpha_{ss}(\omega)d})wI_s \\ K_{ssQ} &= \frac{2\sigma_{ssQ}}{c\epsilon_0\sqrt{\epsilon_r}}\end{aligned} \tag{6}$$

where α_{ss} is the absorption coefficient, R_{ss} is reflection ratio, I_s is the light intensity for light polarization direction s, w is the width of the crystal surface exposed to illumination, d is depth of the crystal, and ϵ_r is dielectric constant. For a bulk crystal, e.g. $BaTiO_3$, the depth d is much larger than length scale of inverse absorption coefficient α_{ss}^{-1} (hundreds of Å), and the total current is

$$J_{ssQ} = \frac{\sigma_{ssQ}}{\alpha_{ss}(\omega)}(1-R_{ss})wE_s^2 = G_{ssQ}(1-R_{ss})wI_s \tag{7}$$

where G_{ssQ} is the Glass coefficient[9]. The absorption coefficient is calculated using $\alpha(\omega)=\frac{\omega}{c}\sqrt{2\sqrt{\epsilon_1^2+\epsilon_2^2}-2\epsilon_1}$, where ϵ_1 and ϵ_2 are obtained from the BSE calculations. In Appendix B, The derivations of absorption coefficient and Glass coefficient are presented[49,50].

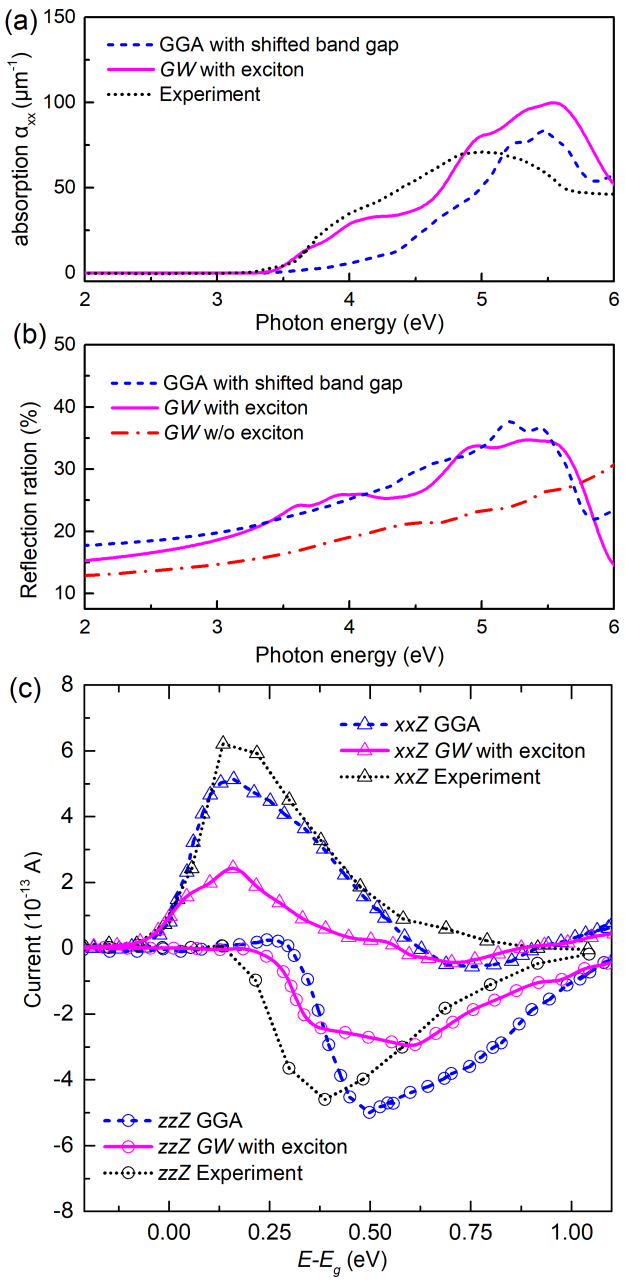

FIG. 3. For $BaTiO_3$, (a) the experimental[48] and computed absorption spectra as a function of photon energy. (b) The reflection ration computed with GGA, GW with exciton, and GW without exciton. The GGA absorption spectrum and reflection ratio are shifted to the experiment band gap. (c) The experimental current[7] and GGA current and GW with exciton correction current, for transverse (xxZ) and longitudinal (zzZ) electric field orientation, as a function of energy above their respective band gaps. The solid and dashed lines are calculated results for a choice of experimental parameters of 0.5 mW/cm^2 illumination intensity and 0.15 cm sample width. Fig.3c shows that while the DFT-level calculation of shift current agrees with experimental measurements, the GW+BSE-level calculation does not. This highlights the importance of mechanisms beyond shift current for the BPVE.

From Eq.(6), we see that the shift current is highly dependent on the absorption coefficient for bulk materials. For bulk single-crystal BTO, the experimental absorption coefficient from Ref.[48] is compared to the coefficients computed using GGA and GW with exciton effects, shown in Fig 3a. Even with a shift of the GGA absorption spectrum to the experimental band gap, it is still qualitatively incorrect compared to experiment. The absorption coefficient is highly underestimated by the GGA calculation, while the GW with exciton correction gives much better absorption coefficient. The enhancement of ϵ_2 near the band edge induced by exciton significantly influences absorption; the $\alpha(\omega)$ with exciton effects is larger than without, for photon energies within 1 eV above the band gap. Besides the absorption coefficient, the reflection ratio (or reflectivity), calculated from dielectric constant, is also influenced by excitons (see Appendix B). For the reflection ratio in BTO, experimental results suitable for quantitative comparison could not be located. However, the reflection ratio measured using unpolarized light and an unpoled sample is around 22%-30%[48] within 1 eV above band gap, which is agree well with our GW calculation with exciton (Fig 3b). We also shift the GGA reflectivity to the experimental band gap. The GGA reflectivity is not very different from the GW with exciton correction. So the shift current difference between GGA and GW with exciton correction in BTO is dominated by the absorption coefficient correction.

In Fig 3c, the experimental current response[7] is compared to the shift current computed using GGA and GW with exciton correction, using the light intensity 0.5 mW/cm^2 and crystal dimensions 0.15 cm of the experiment[7,8]. The GW with exciton correction improves the energy alignment of transvers current (xxZ) response. However, the magnitude of the current including exciton effect is around half of the experimental value. Finally, we note that the exciton effect correction is not updated for shift current conductivity tensor in this work. It is possible that the shift current conductivity tensors can be enhanced by the exciton effect[51] which may eliminate the difference between theory and calculation. However, other mechanisms, such as ballistic-current mechanism, may also contribute to the total DC current. Thus, it is worth to study the physical origins of the DC current in detail.

IV. TOTAL SHIFT CURRENT WITH EXCITON EFFECT IN TWO DIMENSIONAL FERROELECTRICS

Next, we consider the excitonic effects in two-dimensional semiconductor SnSe. We use Coulomb slab truncation and 35 Å vacuum in the GW and exciton calculations, which was sufficient for convergence (see Appendix A). Fig 4(a) and (b) show the absorption coefficient and reflection ratio at different levels of calculation, with similar features as for BTO. The absorption coef-

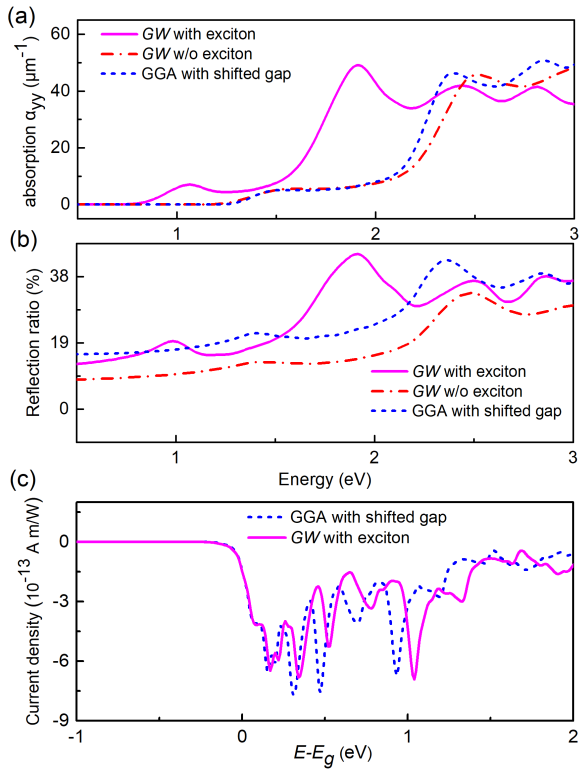

FIG. 4. For two dimensional SnSe, (a) the absorption coefficient is computed at the GGA level, GW level, and GW with exciton correction and (b) reflection ratio, for longitudinal (yy) electric field orientation, as a function of photon energy. (c) the shift current density, for longitudinal (yy) electric field orientation, at GGA level and GW with exciton correction as a function of energy above the GW band gap. For comparison, we estimate the thickness of SnSe to be 5.5 Å. The GGA spectra in each panel are shifted to the GW band gap.

ficient with excitonic effects is enhanced near the band gap, and the reflection ratio including GW with exciton is renormalized, compared with GGA calculations. Nevertheless, these renormalizations do not have a strong effect on the photocurrent of two-dimensional SnSe because its thickness d (5.5 Å) is much smaller than the inverse absorption coefficient, e.g. $\alpha_{yy}^{-1} = 2000$ Å for 1.41 eV light. So, Eq.(5) is reduced to $J_{ssQ} = K_{ssQ}(1 - R_{ss})dwI_s$ for two-dimensional materials. As a result, excitonic effects on the absorption coefficient has a weak influence on the shift current of two-dimensional materials. The overall shift current density (Fig 4c) with exciton is renormalized and slightly reduced from the GGA calculated shift current, caused by the renormalized reflectivity due to excitons and band stretching due to quasiparticles. Importantly, the small reduction in the magnitude of the shift current near the band edge implies that the exciton effect plays much less role in this case and the reason is that the optical penetration depth is much larger than the thickness of the material.

V. CONCLUSIONS

In this work, we have demonstrated that many-body effects lead to significant changes in the shift current response. Quasiparticle GW corrections lead to shifts in peak position and reductions in shift current magnitude, while excitonic effects on the absorption and reflection result in rearrangements of spectral weight, reducing shift current response near the band gap. These results have consequences for our understanding of the role of shift current in the BPVE, and our assessments of the performance of shift current materials. Comparisons of our calculations on $BaTiO_3$ with experiments indicate the magnitude of shift current is only half of the measured anomalous photocurrent. Taking the many-body effects into account, our calculations indicate that the other mechanisms such as ballistic current are likely to play a role in the BPVE, suggesting the possible new physics of photocurrent generation in noncentrosymmetric semiconductor. In addition, the two-dimensional SnSe calculations reveal that excitons have very small influence near and above the band gap, suggesting in-plane two-dimensional or thin film geometries can optimize the materials for BPVE application.

ACKNOWLEDGMENTS

R. F. thank Wenjie Dou and Shiyuan Gao for valuable discussions. This work was supported by the U.S.Department of Energy, Office of Basic Energy Sciences,under Grant No. DE-FG02-07ER46431. The authors acknowledge computational support from the NERSC of the DOE.

Appendix A: Computational details

1. GGA level and shift current

DFT calculations were conducted using a plane-wave basis with a 50 Ry energy cutoff with norm-conserving pseudopotentials for both $BaTiO_3$ and monolayer SnSe. For bulk $BaTiO_3$, an $8 \times 8 \times 8$ Monkhorst-Pack k grid for self-consistent evaluation of the charge densities. Monkhorst-Pack k grid of $24 \times 24 \times 24$, $48 \times 48 \times 48$ and $64 \times 64 \times 64$ are used to ensure a well-converged shift current response. For 2D SnSe, the structural relaxation self- consistent and non-self-consistent calculations, Monkhorst-Pack k grid of $12 \times 12 \times 1$, $48 \times 48 \times 1$ and $72 \times 72 \times 1$ are used to ensure a well-converged shift current response.

2. Many body calculations

The static polarizability and the inverse dielectric matrix are calculated using the static RPA polarizability

using the following expression:

$$\chi_{GG'}(q,0) = \sum_{v}^{occ}\sum_{v}^{emp}\sum_{k} M^{*}_{cv}(k,q,G)M_{vc}(k,q,G') \frac{1}{E_v(k+q) - E_c(k)} \quad \text{(A1)}$$

where

$$M_{cv}(k,q,G) = \langle c, k+q | e^{i(q+G)\cdot r} | v, k \rangle \quad \text{(A2)}$$

are the plane-wave matrix elements. Here q is a vector in the first Brillouin zone, G is a reciprocal lattice vector.

For the GW calculation of intrinsic monolayer SnSe, to get a converged inverse dielectric matrix, the dielectric matrix is calculated on a $36\times36\times1$ with a summation of Nc=120 empty bands (Nv = 12 valence bands) and a cutoff of 8 Ry. The same number of bands are used in the summation of the self-energy with the static reminder approximation to accelerate convergence. A truncation to the Coulomb interaction is applied to eliminate interactions between periodic images. The BSE is solved on a finer $72 \times 72 \times 1$ k-grid. To get converged absorption for photon energy below 8 eV, 6 conduction bands and 9 valence bands are used for the BSE kernel and exciton absorption.

For the GW calculation of tetragonal $BaTiO_3$, the dielectric matrix is calculated on a $24 \times 24 \times 24$ with a summation of Nc=200 empty bands (Nv = 20 valence bands) and a cutoff of 8 Ry. The same number of bands are used in the summation of the self-energy with the static reminder approximation to accelerate convergence. The BSE is solved on a finer $48 \times 48 \times 48$ k-grid. To get converged absorption for photon energy below 10 eV, 9 conduction bands and 9 valence bands are used for the BSE kernel and exciton absorption calculation.

3. Bandstructure and band width

In Fig S1a, we plot the GGA and GW band structure of BTO. The GW bandstrure is not rigid shift of the GGA bands, as shown in Fig S1b. The slopes in Fig S1(b) shows the band widths are changed by the GW correction. The yellow circle in Fig S1(b) shows that the *GW* correction is not a uniform shift and rescaling, as there is a group of bands that does not fit to a scissors operator (starting from the fifth conduction band in S1a).

In Fig S2, the bandstructures at GGA and *GW* level and bandwidths changes are given. Compared with bulk BTO, the bandwidths correction induced by *GW* correction is smaller. Here, the *GW* valence and conduction bandwidth increases by 13% and 8%, respectively.

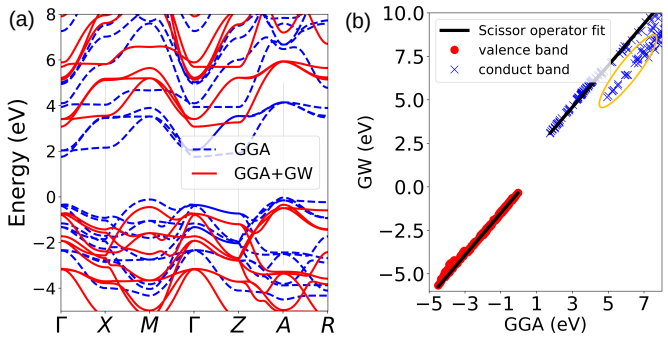

FIG. 5. The bandstructure of tetragonal phase $BaTiO_3$ at GGA level and *GW* level (a), The red solid line and blue dash line represent the band structure at the GW and GGA level, respectively. The energy difference between GGA and *GW* calculation (b), the red dot and blue cross dot represent the valence bands and conduction bands calculations, respectively, the black line is the scissor operator fit, and the yellow circle indicates the scissor approximation is invalid.

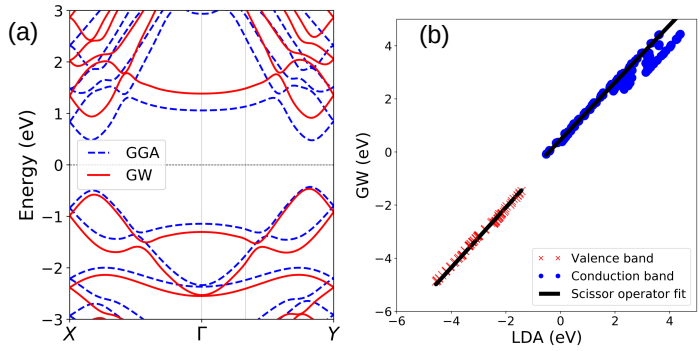

FIG. 6. The bandstructure of two dimensional SnSe at GGA level and *GW* level (a), The red solid line and blue dash line represent the band structure at the *GW* and GGA level, respectively. The energy difference between GGA and *GW* calculation (b), the red cross dot and blue dot represent the valence bands and conduction bands calculations, respectively, the black line is the scissor operator fit, the slope represents the changes of bandwidths

4. Dielectric constant for two dimensional materials

For two dimensional SnSe, the dielectric constant is strongly dependent on the supercell size. We found 20 Å vacuum distance is not good enough for an accurate calculation of the dielectric constant. Here we use several supercell sizes, shown in Fig. S3, to extract the dielectric constant for SnSe. Fig S3 (c-d) shows the exponential decay fitting for the main peaks of the imaginary and real parts of dielectric constant. Using these fitting parameters, we can extract the dielectric of SnSe with an infinite amount of vacuum. The value is very close to the dielectric constant calculated using 35 Å vacuum distance.

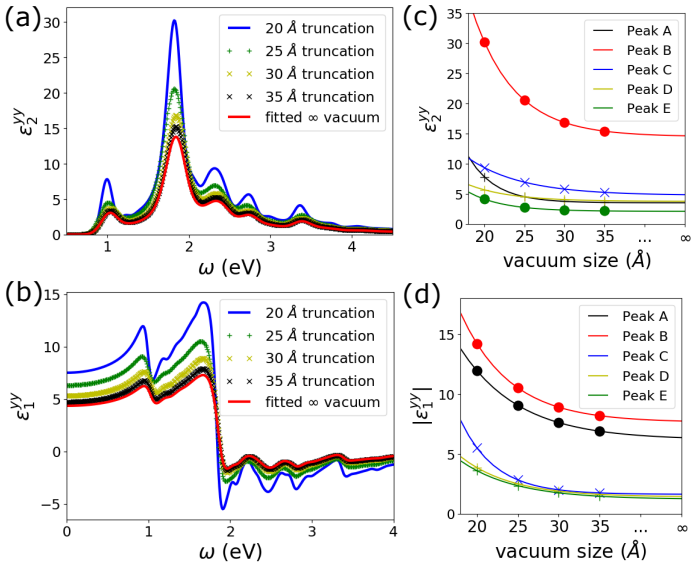

FIG. 7. The imaginary (a) and real part (b) of dielectric constant for two dimensional SnSe. The exponential decay fitting for the peaks of the imaginary (c) and real (d) part of dielectric constant. We use a serial of vacuum distance, e.g. 20, 25, 30, 35 Å, to get get the power law for the dielectric constant.

Appendix B: Derivative for current, absorption coefficient, reflection ratio

1. Complex refraction index and dielectric constant

Using the simple relation between refraction index and complex dielectric constant

$$(a(\omega)+ib(\omega))^2=\epsilon_1+i\epsilon_2 \tag{B1}$$

one can get the complex refraction index by

$$\begin{aligned} a(\omega)&=\sqrt{\frac{1}{2}(\epsilon_1+\sqrt{\epsilon_1^2+\epsilon_2^2})}\\ b(\omega)&=\frac{\epsilon_2^2}{\sqrt{2(\epsilon_1+\sqrt{\epsilon_1^2+\epsilon_2^2})}} \end{aligned} \tag{B2}$$

where the $\epsilon_1(\omega)$ and $\epsilon_2(\omega)$ are the real and imaginary part of complex dielectric constant, respectively. Applying the linear response theory to the first order electric optical interaction[49], the imaginary part $\epsilon_2(\omega)$ is calculated by[38]

$$\epsilon_2(\omega)^{GGA}=\frac{16\pi e^2}{\omega^2}\sum_{c,v}|\langle v|\vec{v}|c\rangle|^2\delta(\omega-(E_c-E_v)) \tag{B3}$$

where we set $\hbar=1$, $\langle v|\vec{v}|c\rangle$ is velocity matrix between conduction band $|c\rangle$ and valence band $|v\rangle$ calculated from GGA approximation. When considering the quasi-particle correction

$$\langle v|\vec{v}|c\rangle^{GW}=\frac{E_c^{GW}-E_v^{GW}}{E_c^{GGA}-E_v^{GGA}}\langle v|\vec{v}|c\rangle^{GGA} \tag{B4}$$

The effect of this renormalization is that, taking into account the division by ω^2, the weight of a transition is not changed when the transition is shifted to higher energies by the GW correction.

If considering the exciton effect in dielectric constant,

$$\epsilon_2(\omega)^{GGA}=\frac{16\pi e^2}{\omega^2}\sum_S|\langle 0|\vec{v}|S\rangle|^2\delta(\omega-\Omega^S) \tag{B5}$$

where the correlated e-h excitation S of energy Ω^S is expanded on the basis of e-h pairs $|S\rangle=\sum A^S_{vc\mathbf{k}}|vc\mathbf{k}\rangle$. Next using the simple Kramers-Krönig relation, the real part $\epsilon_1(\omega)$ is

$$\epsilon_1(\omega)=1+\frac{2}{\pi}p\int_0^\infty d\omega'\frac{\omega'\epsilon_2(\omega)}{\omega'^2-\omega^2} \tag{B6}$$

2. Absorption coefficient

Considering a monochromatic electromagnetic wave propagate in material,

$$\begin{aligned} E_y&=E_0e^{i\omega(\frac{n(\omega)}{c}z-t)}=E_0e^{i\omega(\frac{a(\omega)+ib(\omega)}{c}z-t)}\\ &=E_0e^{-\frac{b(\omega)\omega}{c}z}e^{i\omega(\frac{a(\omega)\omega}{c}z-t)} \end{aligned} \tag{B7}$$

where c is speed of light, $n(\omega)=a(\omega)+ib(\omega)$ is the complex refraction index. Since the light intensity is proportional to E^2, the intensity decay as a factor $e^{-\frac{2\omega b(\omega)}{c}z}$, thus the absorption coefficient $\alpha(\omega)$ is

$$\begin{aligned} \alpha(\omega)&=\frac{2\omega b(\omega)}{c}=\frac{\omega\epsilon_2(\omega)}{a(\omega)c}\\ &=\frac{\omega}{c}\sqrt{2}\sqrt{\sqrt{\epsilon_1^2(\omega)+\epsilon_2^2(\omega)}-\epsilon_1(\omega)} \end{aligned} \tag{B8}$$

3. Reflection coefficient and Reflection ratio

The normal incidence reflectivity (reflection ratio) R is written as[50]

$$\begin{aligned} R&=|\frac{E_{ref}}{E_{in}}|^2=|\frac{1-n(\omega)}{1+n(\omega)}|^2\\ &=\frac{(a(\omega)-1)^2+b(\omega)^2}{(a(\omega)+1)^2+b(\omega)^2} \end{aligned} \tag{B9}$$

and the reflection coefficient for the wave itself is given by

$$r=\frac{1-a(\omega)-ib(\omega)}{1+a(\omega)+ib(\omega)} \tag{B10}$$

where the reflectivity (or reflection ratio) R is a number less than unity and r has an amplitude of less than unity. We have now related one of the physical observables to the optical constants. To relate these results to

the power absorbed and transmitted at normal incidence, we utilize the following relation which expresses the idea that all the incident power is either reflected, absorbed, or transmitted

$$1 = R + A + T \tag{B11}$$

where R, A, and T are the fraction of the power that is reflected, absorbed, and transmitted, respectively.

4. shift current for bulk and two dimensional materials

For a material with d thickness, the shift current is

$$\begin{aligned} J_{ssQ}(\omega) \cdot d \cdot w &= \int_0^d K_{ssQ}(1-R)e^{-\alpha_{ss}(\omega)z} \cdot dz \cdot w \cdot E_s^2 \\ &= \frac{K_{ssQ}}{\alpha_{ss}(\omega)}(1-R_{ss})(1-e^{-\alpha_{ss}(\omega)d}) \cdot w \cdot I_s \end{aligned} \tag{B12}$$

For bulk crystal e.g. $BaTiO_3$, the depth d is much larger than length scale of inverse absorption coefficient α_{ss}^{-1} (hundreds μm), the total current is

$$J_{ssQ} = \frac{\sigma_{ssQ}}{\alpha_{ss}(\omega)}(1-R_{ss}) \cdot w \cdot E_s^2 = G_{ssQ}(1-R_{ss}) \cdot w \cdot I_s \tag{B13}$$

where G_{ssQ} is the Glass coefficient[9]. For very 2D material, e.g. 2D SnSe, the total current is

$$J_{ssQ} = \sigma_{ssQ} d(1-R_{ss}) w E_s^2 = K_{ssQ} d(1-R_{ss}) \cdot w \cdot I_s \tag{B14}$$

* rappe@sas.upenn.edu

[1] V. Belinicher and B. Sturman, Physics-Uspekhi **23**, 199 (1980).
[2] P. J. Sturman, *Photovoltaic and Photo-refractive Effects in Noncentrosymmetric Materials*, Vol. 8 (CRC Press, 1992).
[3] A. Glass, D. v. d. Linde, and T. Negran, *Landmark Papers On Photorefractive Nonlinear Optics*, , 371 (1995).
[4] N. Laman, M. Bieler, and H. Van Driel, Journal of applied physics **98**, 103507 (2005).
[5] J. E. Sipe and A. I. Shkrebtii, Phys. Rev. B **61**, 5337 (2000).
[6] A. G. Chynoweth, Phys. Rev. **102**, 705 (1956).
[7] W. Koch, R. Munser, W. Ruppel, and P. Würfel, Solid State Communications **17**, 847 (1975).
[8] W. Koch, R. Munser, W. Ruppel, and P. Würfel, Ferroelectrics **13**, 305 (1976).
[9] A. Glass, D. Von Der Linde, and T. Negran, Applied physics letters **25**, 233 (1974).
[10] V. M. Fridkin and B. Popov, Soviet Physics Uspekhi **21**, 981 (1978).
[11] T. Choi, S. Lee, Y. Choi, V. Kiryukhin, and S.-W. Cheong, Science **324**, 63 (2009).
[12] S. Yang, J. Seidel, S. Byrnes, P. Shafer, C.-H. Yang, M. Rossell, P. Yu, Y.-H. Chu, J. Scott, J. Ager III, *et al.*, Nature nanotechnology **5**, 143 (2010).
[13] J. Seidel, D. Fu, S.-Y. Yang, E. Alarcón-Lladó, J. Wu, R. Ramesh, and J. W. Ager, Phys. Rev. Lett. **107**, 126805 (2011).
[14] S. M. Young, F. Zheng, and A. M. Rappe, Phys. Rev. Lett. **109**, 236601 (2012).
[15] W. Ji, K. Yao, and Y. C. Liang, Advanced Materials **22**, 1763 (2010).
[16] A. Zenkevich, Y. Matveyev, K. Maksimova, R. Gaynutdinov, A. Tolstikhina, and V. Fridkin, Phys. Rev. B **90**, 161409 (2014).
[17] J. E. Spanier, V. M. Fridkin, A. M. Rappe, A. R. Akbashev, A. Polemi, Y. Qi, Z. Gu, S. M. Young, C. J. Hawley, D. Imbrenda, *et al.*, Nature Photonics **10**, 611 (2016).
[18] L. Z. Tan, F. Zheng, S. M. Young, F. Wang, S. Liu, and A. M. Rappe, Npj Computational Materials **2**, 16026 (2016).
[19] R. von Baltz and W. Kraut, Phys. Rev. B **23**, 5590 (1981).
[20] D. E. Parker, T. Morimoto, J. Orenstein, and J. E. Moore, Phys. Rev. B **99**, 045121 (2019).
[21] V. Belinicher and B. Sturman, Soviet physics, Solid state. **20**, 476,481 (1978).
[22] E. Ivchenko, Y. B. Lyanda-Geller, G. Pikus, and R. Y. Rasulov, Soviet physics,Semicoductors **18**, 55 (1984).
[23] V. I. Belinicher and B. I. Sturman, Ferroelectrics **83**, 29 (1988).
[24] F. Zheng, H. Takenaka, F. Wang, N. Z. Koocher, and A. M. Rappe, The journal of physical chemistry letters **6**, 31 (2014).
[25] A. M. Cook, B. M. Fregoso, F. De Juan, S. Coh, and J. E. Moore, Nature communications **8**, 14176 (2017).
[26] B. M. Fregoso, T. Morimoto, and J. E. Moore, Phys. Rev. B **96**, 075421 (2017).
[27] J. Ibañez Azpiroz, S. S. Tsirkin, and I. Souza, Phys. Rev. B **97**, 245143 (2018).
[28] W. Ji, K. Yao, and Y. C. Liang, Phys. Rev. B **84**, 094115 (2011).
[29] S. M. Young and A. M. Rappe, Physical review letters **109**, 116601 (2012).
[30] R. Fei, W. Kang, and L. Yang, Phys. Rev. Lett. **117**,

097601 (2016).
[31] T. Rangel, B. M. Fregoso, B. S. Mendoza, T. Morimoto, J. E. Moore, and J. B. Neaton, Phys. Rev. Lett. **119**, 067402 (2017).
[32] R. Haleoot, C. Paillard, T. P. Kaloni, M. Mehboudi, B. Xu, L. Bellaiche, and S. Barraza-Lopez, Phys. Rev. Lett. **118**, 227401 (2017).
[33] R. von Baltz and W. Kraut, Phys. Rev. B **23**, 5590 (1981).
[34] A. M. Rappe, K. M. Rabe, E. Kaxiras, and J. D. Joannopoulos, Phys. Rev. B **41**, 1227 (1990).
[35] N. J. Ramer and A. M. Rappe, Phys. Rev. B **59**, 12471 (1999).
[36] Z. H. Levine and D. C. Allan, Phys. Rev. Lett. **63**, 1719 (1989).
[37] M. S. Hybertsen and S. G. Louie, Phys. Rev. B **34**, 5390 (1986).
[38] M. Rohlfing and S. G. Louie, Phys. Rev. B **62**, 4927 (2000).
[39] R. Buttner and E. Maslen, Acta Crystallographica Section B **48**, 764 (1992).
[40] S. Sanna, C. Thierfelder, S. Wippermann, T. P. Sinha, and W. G. Schmidt, Phys. Rev. B **83**, 054112 (2011).
[41] M. S. Hybertsen and S. G. Louie, Phys. Rev. Lett. **55**, 1418 (1985).
[42] K. Chang, J. Liu, H. Lin, N. Wang, K. Zhao, A. Zhang, F. Jin, Y. Zhong, X. Hu, W. Duan, *et al.*, Science **353**, 274 (2016).
[43] M. A. Franzman, C. W. Schlenker, M. E. Thompson, and R. L. Brutchey, Journal of the American Chemical Society **132**, 4060 (2010).
[44] G. Shi and E. Kioupakis, Nano letters **15**, 6926 (2015).
[45] H. Zeng, J. Dai, W. Yao, D. Xiao, and X. Cui, Nature nanotechnology **7**, 490 (2012).
[46] D. Xiao, G.-B. Liu, W. Feng, X. Xu, and W. Yao, Physical Review Letters **108**, 196802 (2012).
[47] S. Ishii, S. Iwata, and K. Ohno, Materials transactions **51**, 2150 (2010).
[48] M. Cardona, Physical Review **140**, A651 (1965).
[49] G. Giuliani and G. Vignale, *Quantum theory of the electron liquid* (Cambridge university press, 2005).
[50] M. Dresselhaus, G. Dresselhaus, S. Cronin, and A. Filho, *Solid State Properties: From Bulk to Nano*, Graduate Texts in Physics (Springer Berlin Heidelberg, 2018).
[51] *After this work was completed and posted, we learned the work about shift current tensor with exiton effect using Time-dependent GW, Y-H Chan, D. Qiu, F. Jornada, S. Louie, arXiv:1904.12813*.